Nanoscale Advances

ROYAL SOCIETY OF CHEMISTRY

PAPER

View Article Online
View Journal | View Issue

Cite this: *Nanoscale Adv.*, 2024, **6**, 2722

Controllable synthesis and morphology-dependent light emission efficiency of Zn_2GeO_4 nanophosphors

Miguel Tinoco, *[a] José Miguel Lendínez,[b] José M. González-Calbet, [ac] Bianchi Méndez, [b] Julio Ramírez-Castellanos [a] and Pedro Hidalgo *[b]

Received 8th January 2024
Accepted 2nd April 2024

DOI: 10.1039/d4na00018h

rsc.li/nanoscale-advances

Zn_2GeO_4 is considered a very promising alternative to current luminescent semiconductors. Previous results suggest that its emitted wavelength may depend on different variables, such as particle size and morphology, among others. In this work, we have prepared pure and highly homogeneous Zn_2GeO_4 nanorods under hydrothermal synthesis conditions with a willemite-like structure. Their luminescent properties have been explored and their band gap is estimated, which are distinct from those of previously reported Zn_2GeO_4 bulk particles. Therefore, our results identify particle morphology as a crucial factor for maximizing and fine-tuning the luminescence of Zn_2GeO_4 nano-phosphors.

Introduction

The III–V semiconductors are widely recognized as some of the most significant basic materials for the development of light-emitting devices worldwide, due to their exceptional capabilities.[1] Nevertheless, the semiconductor industry is searching for novel light emitting materials due to the high toxicity of current semiconductors and some of their alternatives, especially those based on arsenic,[2] gallium,[3] or lead.[4] In addition, the production of indium, which is a common element appearing in III–V semiconductors, is highly dependent on the fluctuations of other metal markets as it is only obtained as a byproduct during processing of other metal ores.[5] Apart from that, rare earth elements, which appear in the composition of current phosphors, have been classified as critical raw materials by several international organizations, which have recommended lessening their usage in industry.[6,7] All of these factors have intensified the search for novel semiconductor compounds, which may overcome most of these drawbacks.

Ternary oxides, particularly those based on ZnO and TiO_2, have emerged as some of the most promising candidates to replace current light-emitting semiconductors, fulfilling all previous requirements. Furthermore, various synthesis methods can be employed to prepare oxide nanophosphors with an up to standard purity and crystallinity with controlled morphologies and particle sizes, which can be easily tuned by simply modifying synthesis conditions.[8–11]

Among these materials, bulk Zn_2GeO_4 emits in the blue-green region, peaking at 2.39 eV. Nevertheless, its photoluminescence can be considered rather complex as it is the contribution of three different signals, whose maxima occur at 2.28, 2.38 and 2.73 eV respectively.[12] The origin of this visible emission is the presence of donor and acceptor centres related to native defects. Oxygen vacancies and/or zinc interstitials play the donor role, while germanium and/or zinc vacancies the acceptor one. The maxima position agrees with Density Functional Theory (DFT) calculations that reported the energy levels of point defects in Zn_2GeO_4.[13,14]

In addition to the intrinsic features of defect microstructure, particle size and shape, or crystallographic anisotropy, are widely known to be intertwined with many parameters, having a considerable effect on the physicochemical characteristics of nanoparticles (NPs).[15] However, to the best of our knowledge, no exhaustive study of the variations of Zn_2GeO_4 luminescence by comparing these parameters has been carried out yet. Nevertheless, preliminary results evidence that Zn_2GeO_4 nanoparticles emit different wavelengths depending on their morphology and particle size. In particular, hexagonal microrods emit at 2.03, 2.40 and 2.86 eV,[16] and nanowires at 1.89, 2.11 and 2.34 eV,[17] whilst small nanoparticles present luminescence signals at 2.4, 2.7 and 3.1 eV.[18] Therefore, such remarkable variations imply that particle size and morphology may affect Zn_2GeO_4 luminescence, as it happens in other materials such as Si.[19] Nevertheless, information about the optical properties of more types of undoped Zn_2GeO_4 particles is fairly limited. Covering a broader range of nanoparticle shapes and sizes may help to correlate the emitted light with different characteristic

[a]*Departamento de Química Inorgánica, Facultad de Ciencias Químicas, Universidad Complutense de Madrid, Madrid, 28020, Spain. E-mail: mitinoco@ucm.es; Tel: (+34)913948502*

[b]*Departamento de Física de Materiales, Facultad de Ciencias Físicas, Universidad Complutense de Madrid, Madrid, 28020, Spain. E-mail: phidalgo@ucm.es; Tel: (+34)913944790*

[c]*ICTS National Center for Electron Microscopy, Universidad Complutense de Madrid, Madrid, 28020, Spain*

features of Zn_2GeO_4 crystallites with the ultimate goal of generating toxic-free nanophosphors with tunable properties. Therefore, a synthesis route that provides accurate control of the morphology and size would be quite advisable for applications that require some kind of luminescence tuning.

Several studies have reported the preparation of Zn_2GeO_4 nanoparticles with a myriad of morphologies employing diverse synthetic methods. Solvothermal and hydrothermal procedures stand out among these methodologies due to the fine morphological and particle size control they provide. In particular, numerous articles report the solvothermal synthesis of Zn_2GeO_4 nanorods, commonly applied as photocatalysts,[20,21] for biosensing,[22] and for lithium batteries.[23,24] Apart from that, Zn_2GeO_4 ultrathin nanoribbons[25] can also be obtained following a hydrothermal method, while other procedures can be employed to prepare Zn_2GeO_4 with different morphologies: CVD (nanowires),[26–29] ceramic (polycrystals),[30] template-assisted method (hollow spheres),[31] *etc.*

In this article we report the reproducible hydrothermal synthesis of short Zn_2GeO_4 nanorods for light-emitting applications. An exhaustive structural, morphological and luminescence characterization study was conducted, which allowed us to correlate the optoelectronic properties of this material with its morphological aspects, which is of maximum importance for its possible technological applications.

Experimental

Synthesis

Zn_2GeO_4 nanoparticles were synthesized following a conventional hydrothermal method. In a typical synthesis, 0.1 g of GeO_2 (Sigma-Aldrich, 99.9%) was dissolved in a 0.33 M NaOH solution (Sigma-Aldrich, 98%) under continuous stirring. A stoichiometric amount of a 0.04 M $Zn(CH_3COO)_2 \cdot 2H_2O$ (Merck, 99.5%) solution was added dropwise and the resulting mixture was poured into a Teflon-line stainless steel autoclave. The autoclave was kept in an oven for 12 h at 100 °C. The as-obtained white precipitate was centrifuged, washed several times with water until pH = 7, and dried overnight. The synthesis was carried out several times to verify the reliability of the results obtained.

Structural characterization

X-ray diffraction (XRD) measurements were performed on a Bruker D8 ADVANCE A25 diffractometer equipped with a Cu tube and Bragg–Brentano optics with fixed slits, a Ni filter and a position sensitive LynxEye SSD160-2 detector. Patterns were recorded within the 2θ range of 5–80°, using a step size of 0.01° and a collection time of 1 s per step.

Transmission electron microscopy (TEM) experiments were conducted using a JEOL JEM 2100 microscope, located in the facilities of the National Centre of Electron Microscopy (ICTS-CNME). The spatial resolution achieved operating at 200 kV in High Resolution Transmission Electron Microscopy mode (HRTEM) is 0.25 nm. Zn_2GeO_4 nanoparticles were dispersed into 1-butanol by sonication for 5 minutes prior to their deposition onto the holey-carbon copper grid to reduce their agglomeration. A crystallographic model of the Zn_2GeO_4 structure has been created using the free software Vesta from JP-Minerals.

Photoluminescence measurements

A Horiba Jobin Ybon LabRaman Hr800 confocal microscope using a 325 nm He–Cd laser as the excitation source was used for photoluminescence (PL) measurements at room temperature (RT). An Edinburgh Instruments FLS1000 system, equipped with a 450 W Xe lamp and a helium cryostat, was employed for acquiring photoluminescence–photoluminescence excitation (PL–PLE) spectra from 4 K up to RT.

Results and discussion

Structural and morphological characterization

XRD was carried out on the as-synthesized nanoparticles, whose diffraction pattern is displayed in Fig. 1. All the diffraction peaks were perfectly indexed on the rhombohedral space group $R\bar{3}$ basis of Zn_2GeO_4 (ICSD Collection Code: 68382), with cell parameters $a = b = 14.28$ Å and $c = 9.55$ Å. This diffractogram clearly shows that nanocrystals possess a willemite-like structure[32] compared to the Zn_2GeO_4 reference, where the structure can be described as formed of tetrahedrally coordinated zinc and germanium atoms, sharing corners.[33] The absence of additional reflections, which could be attributed to impurities, is indicative of the remarkable purity of the Zn_2GeO_4 sample, even without the need for high-temperature thermal treatments. The relative wide maxima suggest the nanoparticle nature of the material.

The average crystal size has been calculated from the values of the form factor K, the wavelength of the incident radiation λ, the full width at half maximum B, the diffraction maximum

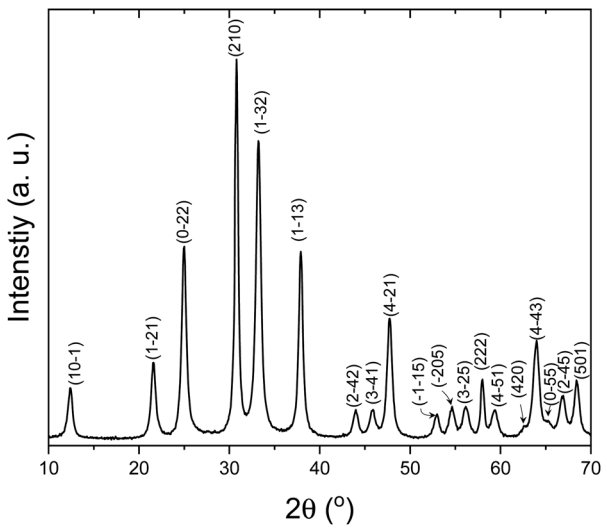

Fig. 1 Indexed XRD pattern of the as-synthesized Zn_2GeO_4 nanoparticles.

{210}, and the diffraction angle θ, along with the Scherrer formula: $D = K\lambda/(B\cos\theta)$. The mean value is 17 ± 0.02 nm.

To confirm these results, transmission electron microscopy studies have been carried out. The low-magnification TEM image depicted in Fig. 2a evidences that most nanoparticles possess a short rod-like morphology. Particle length and diameter distributions are presented in Fig. 2b and c, revealing their small size. Specifically, particle length ranges between 24 and 54 nm with an average length of 37 ± 7 nm, whilst their mean diameter stands at 13 ± 3 nm, varying from 7 to 19 nm. These values provide an aspect-ratio value of 1 : 3 for the nanorods. Particle size distributions have been constructed measuring 50 different nanoparticles.

In addition, our HRTEM studies confirm that the structure of the nanorods corresponds to rhombohedral willemite-like Zn_2GeO_4. Fig. 2d and f depict the electron micrograph top-view images of representative agglomerates of Zn_2GeO_4 nanocrystals oriented along the [001] zone axis. As suggested by these images, the radial morphology of these rod-like nanoparticles is greatly varied, but numerous cross-sections present 60° and 120° angles. Therefore, some of these nanoparticles may derive from distorted hexagonal and truncated triangular prismatic nanocrystals.

The digital diffraction pattern (DDP), extracted from one of the crystals (Fig. 2e) clearly shows the perfect willemite-like lattice of the nanocrystals. The reflection distances and angles measured are 3.6 Å at 60°, corresponding to {200}, {020} and {1−10} planes oriented along the [001] zone axis. On the other hand, the characteristic tunnels, inherent to the willemite structure and parallel to the [001]-axis direction, which are clearly observed in the graphical representation of the Zn_2GeO_4 structure displayed in Fig. 2h, can be readily discerned in Fig. 2g, which depicts a magnified region from Fig. 2f. The experimental diameter of the tunnels has been estimated using HRTEM images, and the measured values are approximately 7.3 Å, in accordance with the structure described for this oxide.[32]

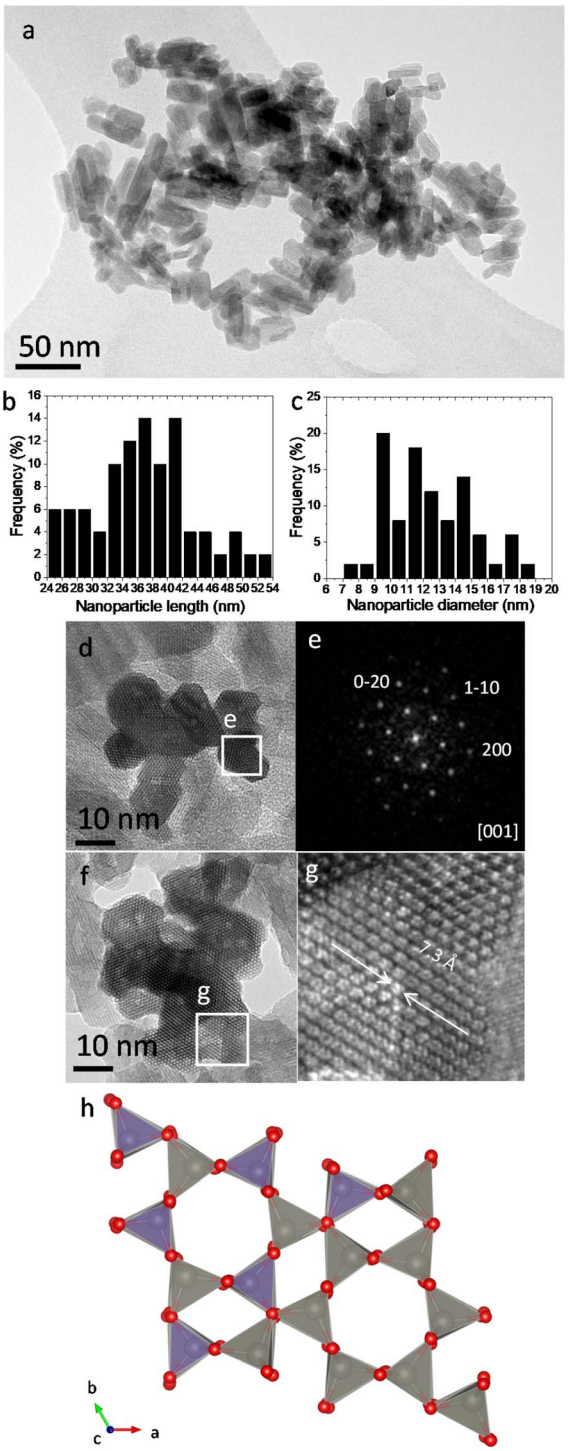

Fig. 2 (a) Representative low magnification TEM image of the as-synthesized Zn_2GeO_4 nanoparticles. (b) and (c) Nanoparticle length and diameter distributions, respectively. (d) HRTEM top-view image of a Zn_2GeO_4 nanoparticle agglomerate. (e) DDP extracted from the region encircled in (d). (f) HRTEM top-view image of another Zn_2GeO_4 nanoparticle agglomerate, from which a magnified inset was extracted (g), evidencing the presence of the characteristic tunnels of the willemite-type structure of Zn_2GeO_4. (h) Crystallographic model of the Zn_2GeO_4 structure viewed along the [001] zone axis.

Optical characterization of the nanoparticles

An in-depth study of the luminescence emission of the as-synthesized Zn_2GeO_4 nanoparticles was carried out. An analysis of the emission provides information about the electronic recombinations between conduction and valence bands or between the electronic levels caused by native defects within the bandgap. As a first step, room temperature luminescence of these Zn_2GeO_4 nanocrystals has been assessed. Fig. 3 shows the room temperature luminescence spectrum acquired with an He–Cd laser (λ = 325 nm). A broad visible band covering practically the whole visible range is observed. PL spectra agree with the complex nature of the luminescence band involving several radiative centres. The broad luminescence emission can be deconvoluted intro three components (2.18 eV, 2.41 eV and 2.81 eV), as previously reported in other Zn_2GeO_4 nanoparticles grown by a different synthesis method.[18] The green-yellow broad band whose maximum is centred at 2.41 eV is the dominant contribution to the luminescence of this material. Li and co-workers[34] have suggested that this complex band is

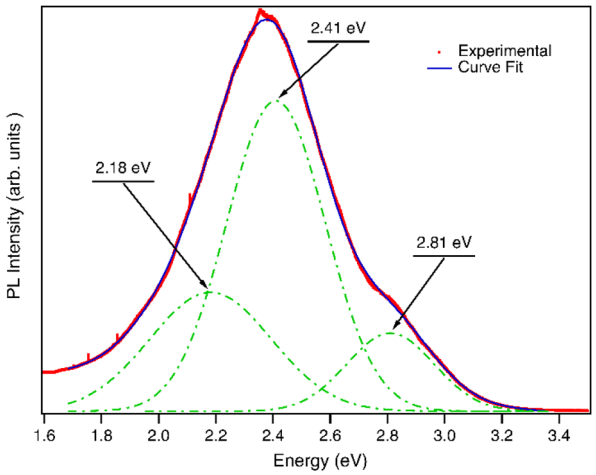

Fig. 3 RT luminescence spectra from Zn_2GeO_4 nanorods excited by a 325nm UV laser. Gaussian emission bands after deconvolution (dotted lines) are shown.

related to Ge centres (bands peaked at 2.18 eV and 2.41 eV) and oxygen defects (band peaked at 2.8 eV).

These emission contributions are very close to the ones reported for microrods, which have overall higher dimensions (1–2 microns wide and hundreds of microns length),[16] and rather distinct from Zn_2GeO_4 nanoparticles, nanowires and Zn_2GeO_4 in bulk form.[17,18,35]

Particularly, the aspect ratio between the microrods prepared in our previous work[16] and these nanorods is rather similar, but their overall dimensions are entirely distinct. Nevertheless, the nanoparticle size of the sample we synthesized in a previous paper[18] (10 or 16 nm in average) is comparable to some of our nanorods, but with an aspect ratio close to 1 : 1. Hence, our results evidence that particles with similar morphologies, but clearly different particle sizes (nanorods and microrods) possess an analogous phosphor emission, which reinforces the relevant effect of morphology on the light emission efficiency of Zn_2GeO_4. Therefore, particle size preliminarily seems to play a minor role in the light emitting properties than particle morphology. Hence, by reducing the particle size we can provide several of the advantages of nanoparticles *versus* micro and bulk materials without drastically altering the luminescent response of the material.

This occurrence might be explained assuming the absence of charge carriers' confinement along the *c* zone axis in nanorods and microrods (due to their length) while this confinement is present along all crystallographic directions in Zn_2GeO_4 nanoparticles. The crystallographic anisotropic character of Zn_2GeO_4 could further reinforce this hypothesis. In this sense, previous literature has evidenced that Zn_2GeO_4 optical properties along the *c* axis, such as its refractive index and Raman signals, differ from the ones measured at the basal plane.[36] Additionally, the competition between surface states and "volume" electronics sates would also affect the luminescence behaviour.

To understand better the origin of these emission bands, PL and PLE spectra were acquired at RT and at low temperature (4 K). Fig. 4 shows the contour plot PL–PLE mappings recorded at

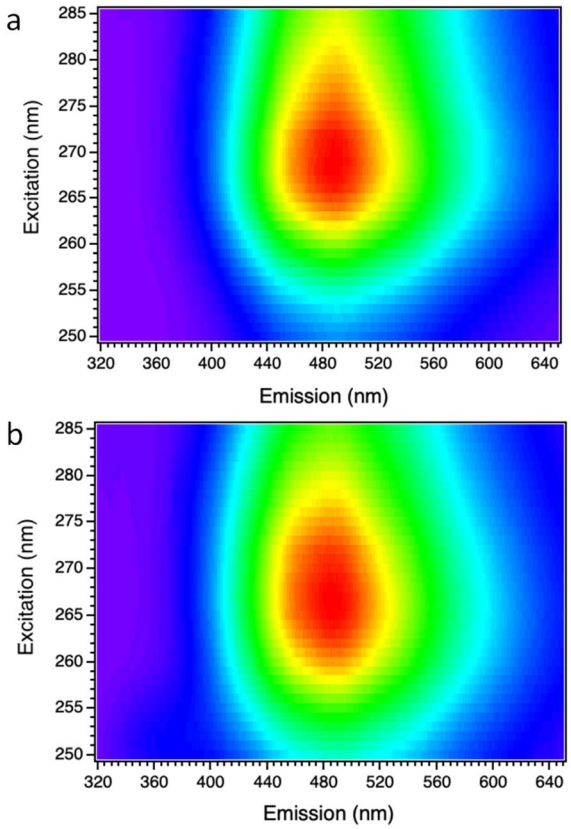

Fig. 4 PL–PLE maps acquired on the nanorods (a) at RT and (b) at 4 K. The color code employed for representing the relative PL–PLE intensity follows a rainbow-like trend: red corresponds to the highest normalized intensity, while violet pixels represent emission energies with the lowest relative intensities.

RT (Fig. 4a) and 4 K (Fig. 4b). In both cases, spectra were collected by varying the excitation wavelength between 250 and 285 nm (4.96–4.35 eV) in order to ensure an excitation energy over, or close to the bandgap energy to be used, while the light emitted was recorded between 320 and 650 nm (3.88–1.9 eV).

Analysing the data from these emission maps, a broadening of the emission spectra occurs as temperature increases, along with a decrease of the overall luminescence intensity. Furthermore, it can be observed that the maximum emission of the sample occurs with an excitation in the range of 265–270 nm for 4 K, and that this range increases to 260–280 nm when the sample is at RT. Using an excitation with an energy above the gap of the material produces a UV emission centred between 320 and 400 nm (3.1–3.4 eV). Under these excitation conditions, an additional ultraviolet band centred at 3.4 eV is observed at low temperature. This band has been previously attributed to a recombination between V_O related electronic levels and self-trapped holes.[12] Therefore, the intensity of this band is directly related to oxygen vacancies. The overall PL spectrum observed in Fig. 5a is not composed of a unique emission band as shown in Fig. 5b. Deconvolution of the PL spectrum at 4 K shows that it is composed of five Gaussian emissions: three in the visible range (2.01 eV, 2.40 eV and 2.68 eV) and two Gaussian emissions in the ultraviolet range (3.11 eV and 3.47 eV), with 2.4

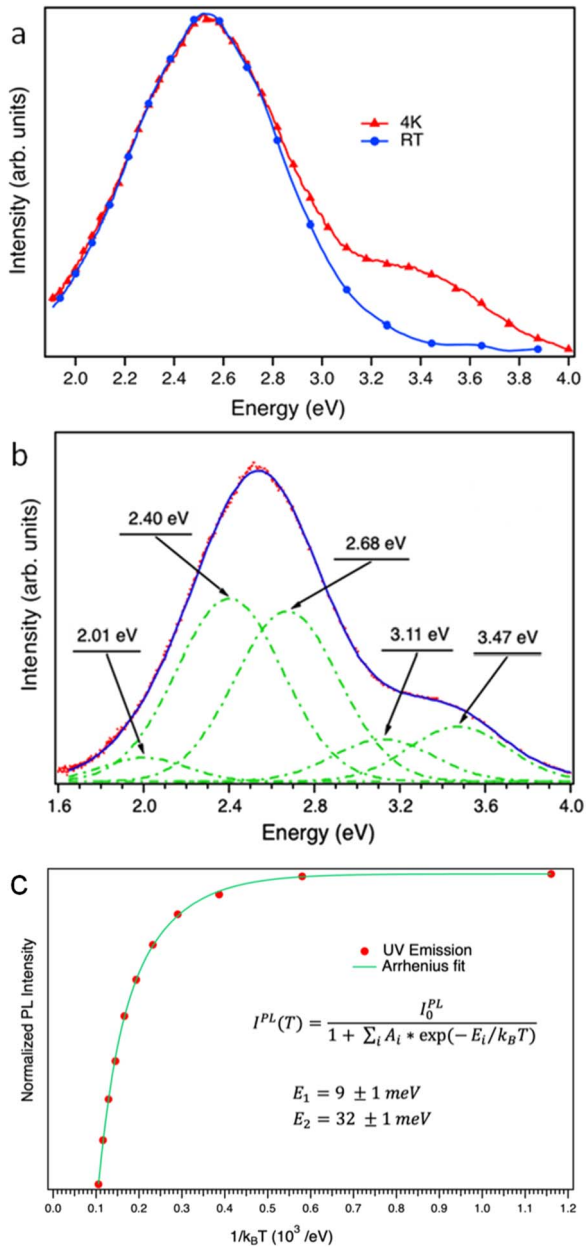

Fig. 5 (a) Luminescence spectra, at 4 K and RT, form nanorods under 250 nm excitation wavelength of a xenon lamp. (b) Gaussian emission bands after deconvolution (dotted lines) of the spectrum acquired at 4 K are shown. (c) Temperature dependence of PL intensity emission.

and 2.68 eV being the most representative in the visible region and 3.47 eV in the UV region. It is worth mentioning that this UV emission is quenched totally at 100–100 K, remaining only the visible band.

The temperature dependence of the PL intensity of emissions related to defect centers can be studied in an Arrhenius-plot scheme. The results for the UV emission are shown in Fig. 5c. From fitting this data to the empirical expression shown in the figure, the activation energies of non-radiative centres affecting the final radiative yield can be estimated. The results show that two levels are required to properly fit the

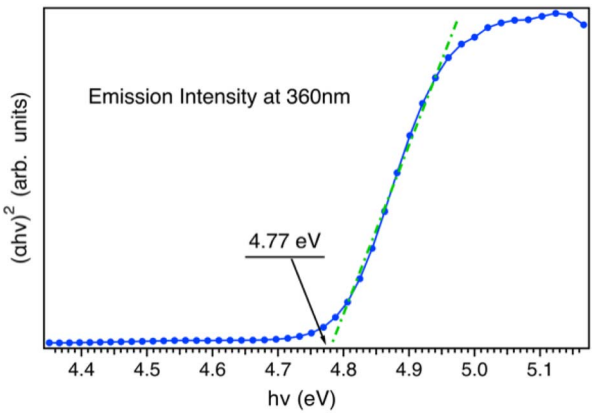

Fig. 6 PLE spectrum at 4 K of the nanorods, from which the optical band gap is estimated.

experimental results, with activation energies of 8 ± 1 meV and 27 ± 1 meV. The channel associated with the lower energy supports an efficient emission at low temperature, but not upon 100 K, and the second channel is not relevant at this temperature range. For comparison, in the case of nanoparticles, values of 17 ± 1 and 84 ± 3 meV were obtained.[18]

Finally, our PL–PLE study allows us to estimate the optical band gap of the nanorods, since it is proportional to the absorption spectrum.[37] Fig. 6 shows the photoluminescence excitation spectrum (PLE) corresponding to the emission of the nanoparticles at 360 nm (3.44 eV) upon varying the excitation wavelength from 240 nm to 285 nm. By fitting the absorption onset, an estimation of the optical band gap of 4.77 eV at 4 K for our nanorods is provided. This value is analogous to that reported for microwires (4.76 eV). However, it is lower than the one reported for nanoparticles (4.85 eV) and thin films (4.9 eV)[39] and higher in comparison with bulk Zn_2GeO_4 (4.68 eV).[38] These results clearly evidence the influence of crystallite morphology on the optoelectronic properties of Zn_2GeO_4 as nanoparticles with radically different external shapes present rather distinctive optoelectronic responses.

Conclusions

Zn_2GeO_4 short nanorods were successfully prepared by a reproducible hydrothermal synthesis. These nanorods are quite homogeneous in both particle size and morphology, with no impurities. A high number of nanostructures with about 1 : 3 aspect ratio are achieved. These nanomaterials become an intermediate step between nanoparticles of few nanometer diameter and nanowires with microns in length. PL spectra collected at both room temperature and at 4 K are rather wide, covering almost all the visible range being centred in the green-yellow region. Deconvolution of PL spectra brings about several components, which are attributed to donor–acceptor pair transitions involving native defects (oxygen vacancies as donors and zinc/germanium vacancies as acceptors). In addition, oxygen vacancies and self-hole traps produce UV emission at low temperatures upon excitation at energies above the

excitation threshold and the emission is quenched around 120 K. The bandgap of Zn_2GeO_4 nanorods has been estimated as 4.77 eV, which is lower than the one reported for nanoparticles and higher in comparison with bulk Zn_2GeO_4. The results strongly reinforce that morphology and aspect-ratio are crucial parameters in the optoelectronic properties of Zn_2GeO_4.

Author contributions

MT and JRC: conceptualization; MT, JML and PH: methodology; MT and PH: formal analysis; MT and PH: investigation; MT and PH: writing – original draft; MT, PH and JRC: writing – review and editing; JMGC and BM: supervision; JMGC and BM: funding acquisition. All authors have read and agreed to the published version of the manuscript.

Conflicts of interest

There are no conflicts to declare.

Acknowledgements

The authors acknowledge the Spanish Ministry of Science and Innovation for funding through Research Projects PID 2020-113753RB-100 and PID2021-122562NB-I00.

Notes and references

1 J. A. Del Alamo, *Nature*, 2011, **479**, 317–323.
2 A. Tanaka, *Toxicol. Appl. Pharmacol.*, 2004, **198**, 405–411.
3 C. R. Chitambar, *Int. J. Environ. Res. Public Health*, 2010, **7**, 2337–2361.
4 M. Leng, Z. Chen, Y. Yang, Z. Li, K. Zeng, K. Li, G. Niu, Y. He, Q. Zhou and J. Tang, *Angew. Chem., Int. Ed.*, 2016, **128**, 15236–15240.
5 A. M. Alfantazi and R. R. Moskalyk, *Miner. Eng.*, 2003, **16**, 687–694.
6 European Commission, *First Commission Interim Report on the Implementation of Pilot Projects and Preparatory Actions 2012*, 2012.
7 US Department of Energy, *U.S. Department of Energy's Strategy to Support Domestic Critical Mineral to Support Domestic Critical Mineral and Material Supply Chain*, 2021.
8 D. V. Bavykin, J. M. Friedrich and F. C. Walsh, *Adv. Mater.*, 2006, **18**, 2807–2824.
9 P. Roy, S. Berger and P. Schmuki, *Angew. Chem., Int. Ed.*, 2011, **50**, 2904–2939.
10 C. B. Ong, L. Y. Ng and A. W. Mohammad, *Renewable Sustainable Energy Rev.*, 2018, **81**, 536–551.
11 Z. L. Wang, *J. Phys.: Condens. Matter*, 2004, **16**, R829.
12 Z. Liu, X. Jing and L. Wang, *J. Electrochem. Soc.*, 2007, **154**, H500.
13 Z. Y. Xie, H. L. Lu, Y. Zhang, Q. Q. Sun, P. Zhou, S. J. Ding and D. W. Zhang, *J. Alloys Compd.*, 2015, **619**, 368–371.
14 J. Dolado, R. Martínez-Casado, P. Hidalgo, R. Gutierrez, A. Dianat, G. Cuniberti, F. Domínguez-Adame, E. Díaz and B. Méndez, *Acta Mater.*, 2020, **196**, 626–634.
15 L. Yang, Z. Zhou, J. Song and X. Chen, *Chem. Soc. Rev.*, 2019, **48**, 5140–5176.
16 P. Hidalgo, A. López, B. Méndez and J. Piqueras, *Acta Mater.*, 2016, **104**, 84–90.
17 J. Xu, C. Wang, Y. Zhang, X. Liu, X. Liu, S. Huang and X. Chen, *CrystEngComm*, 2013, **15**, 764–768.
18 J. Dolado, J. García-Fernández, P. Hidalgo, J. González-Calbet, J. Ramírez-Castellanos and B. Méndez, *J. Alloys Compd.*, 2022, **898**, 162993.
19 H. F. Wilson, L. McKenzie-Sell and A. S. Barnard, *J. Mater. Chem. C*, 2014, **2**, 9451–9456.
20 Q. Liu, Z. X. Low, L. Li, A. Razmjou, K. Wang, J. Yao and H. Wang, *J. Mater. Chem. A*, 2013, **1**, 11563–11569.
21 J. Huang, K. Ding, Y. Hou, X. Wang and X. Fu, *ChemSusChem*, 2008, **1**, 1011–1019.
22 J. Wang, Q. Ma, W. Zheng, H. Liu, C. Yin, F. Wang, X. Chen, Q. Yuan and W. Tan, *ACS Nano*, 2017, **11**, 8185–8191.
23 J. K. Feng, M. O. Lai and L. Lu, *Electrochem. Commun.*, 2011, **13**, 287–289.
24 Y. R. Lim, C. S. Jung, H. S. Im, K. Park, J. Park, W. Il Cho and E. H. Cha, *J. Mater. Chem. A*, 2016, **4**, 10691–10699.
25 Q. Liu, Y. Zhou, J. Kou, X. Chen, Z. Tian, J. Gao, S. Yan and Z. Zou, *J. Am. Chem. Soc.*, 2010, **132**, 14385–14387.
26 Z. Liu, H. Huang, B. Liang, X. Wang, Z. Wang, D. Chen and G. Shen, *Opt. Express*, 2012, **20**, 2982–2991.
27 X. Zhou, Q. Zhang, L. Gan, X. Li, H. Li, Y. Zhang, D. Golberg and T. Zhai, *Adv. Funct. Mater.*, 2016, **26**, 704–712.
28 C. Yan and P. S. Lee, *J. Phys. Chem. C*, 2009, **113**, 14135–14139.
29 Z. Gu, F. Liu, X. Li and Z. W. Pan, *Phys. Chem. Chem. Phys.*, 2013, **15**, 7488–7493.
30 F. Chi, X. Wei, B. Jiang, Y. Chen, C. Duan and M. Yin, *Dalton Trans.*, 2018, **47**, 1303–1311.
31 J. Liu, G. Zhang, J. C. Yu and Y. Guo, *Dalton Trans.*, 2013, **42**, 5092–5099.
32 J. Breternitz, D. Fritsch, A. Franz and S. Schorr, *Z. Anorg. Allg. Chem.*, 2021, **647**, 2195–2200.
33 K.-H. Klaska, J. C. Eck and D. Pohl, *Acta Crystallogr.*, 1978, **34**, 3324–3325.
34 L. Li, Y. Su, Y. Chen, M. Gao, Q. Chen and Y. Feng, *J. Comput. Theor. Nanosci.*, 2010, **3**, 1–5.
35 X. Duan, M. Yuan, K. Ou, W. Zhao, T. Tian, W. Duan, X. Zhang and L. Yi, *Mater. Today Commun.*, 2021, **27**, 102359.
36 J. Dolado, R. Martínez-Casado, P. Hidalgo and B. Méndez, *Opt. Mater. Express*, 2023, **13**, 3156.
37 H. Masai, Y. Yamada, Y. Suzuki, K. Teramura, Y. Kanemitsu and T. Yoko, *Sci. Rep.*, 2013, **3**, 03541.
38 C. Yan, N. Singh and P. S. Lee, *Appl. Phys. Lett.*, 2010, **96**, 053108.
39 S. Luo, L. Trefflich, S. Selle, R. Hildebrandt, E. Krüger, S. Lange, J. Yu, C. Sturm, M. Lorenz, H. Von Wenckstern, C. Hagendorf, T. Höche and M. Grundmann, *Appl. Phys. Lett.*, 2023, **122**, 031601.